Quantitative chemical imaging and unsupervised analysis using hyperspectral coherent anti-Stokes Raman scattering microscopy - Supplementary Material

Francesco Masia,*,† Adam Glen,‡ Phil Stephens,‡ Paola Borri,¶ and Wolfgang Langbein†

School of Physics and Astronomy, Cardiff University, Cardiff, UK, Institute of Tissue Engineering and Repair, School of Dentistry, Cardiff University, Cardiff, UK, and School of Biosciences, Cardiff University, Cardiff, UK

E-mail: masiaf@cf.ac.uk

Materials and Methods

Raman spectroscopy

Raman spectra have been a taken in a home-built Raman micro-spectrometer attached to the same microscope stand as the CARS set-up. The excitation beam was provided by a 50 mW continuous wave laser of 532 nm wavelength and coupled into the microscope by a Semrock LPD01-532RS-25 dichroic beamsplitter. The Raman scattering was collected in

*To whom correspondence should be addressed
†School of Physics and Astronomy, Cardiff University, Cardiff, UK
‡Institute of Tissue Engineering and Repair, School of Dentistry, Cardiff University, Cardiff, UK
¶School of Biosciences, Cardiff University, Cardiff, UK

epi direction, transmitted through the dichroic beamsplitter and a Semrock BLP01-532R-25 long-pass filter, spectrally dispersed by a Horiba Jobin-Yvon iHR550 imaging spectrometer with a 600 l/mm grating, and detected by a Andor Newton DU971N CCD camera, with $2\,\mathrm{cm}^{-1}$ resolution. To enable imaging, the excitation and the detection is confocal, with the detection spatial filter given by the spectrometer input slit ($30\,\mu$m) and a 3 pixels ($48\,\mu$m) vertical range on the CCD in a relayed intermediate image plane of the microscope with a $24\times$ magnification. The spectral sensitivity was determined with a calibration source and corrected in the Raman spectra to represent detected photons per second and wavenumber. The Raman spectra have furthermore been corrected by the factor ν^{-3}, where ν is the frequency of Raman scattered light, to take into account[1] the photon density of states factor in the spontaneous Raman scattering, which is not present in the CARS susceptibility.

Samples

Polystyrene

Polystyrene (PS) grains (Sigma Aldrich, molecular weight $\sim$ 280000) were dissolved in toluene (5% w/w final concentration) and then drop cast on a microscope slide. A #1 coverslip was placed on the solution, to provide and optically flat structure, prior to solvent evaporation. We measured a resulting film thickness of $8\,\mu$m using DIC microscopy.

Glycerol trioleate

Glycerol trioleate (GTO) was sourced from Sigma Aldrich. It is a symmetrical triglyceride derived from glycerol and three units of the unsaturated fatty acid oleic acid. $15\,\mu$l of GTO was pipetted into a well created by the 9 mm diameter opening of a 0.12 mm thick adhesive imaging spacer (Grace BioLabs) attached to a microscope slide, and subsequently capped with a #1 coverslip.

Lipid mixtures

A series of mixtures of octanoic acid and α-linolenic acid from Sigma Aldrich were prepared at different volume concentration. The two fatty acids show distinctive vibrational frequencies as the former is a saturated lipid while the latter is polyunsaturated (see Fig. 2). The samples have been prepared in the same format as GTO.

Cells

Mouse 3T3L1 cells were maintained in DMEM/F12 supplemented with 10% (v/v) foetal bovine serum and 2 mM L-glutamine in a humidified incubator (5% CO_2). Cells were grown until confluent and differentiated for up to 10 days by addition of 85 nM insulin and 2 nM T3 to 3T3L1 maintenance medium with medium being replaced every 48 hours.

IMT11 [2] mouse embryonic stem (mES) cells were maintained in a pluripotent state in alpha MEM supplemented with 10% (v/v) foetal bovine serum (batch tested), 10% (v/v) newborn calf serum (batch tested), 10^{-4} M beta mercaptoehtanol, 2 mM L glutamine and LIF (1000units/ml) (mES media) in a humidified incubator (5% CO_2). The mES cells were differentiated according to a protocol developed by Dani and coauthors. [3] Briefly, mouse ES cells were induced to differentiate by creating embryoid bodies (EBs) via the hanging drop method. This was achieved by spotting 1000 cells/10 μl in a bacteriological dish in mES media without LIF. To create hanging drops bacteriological dishes were inverted atop smaller bacteriological dishes filled with PBS for 2 days. Subsequently were inverted and EB's were treated with mES media supplemented with 10^{-6} M all-trans retinoic acid for 3 days, with media being changed daily. EB's were cultivated for a further 2 days in maintenance media and approximately 2-4 EB's/cm^2 transferred to gelatin (0.1%) coated glass slides and allowed to settle for 12 hours before culturing in mES media supplemented with 85 nM insulin, 2 nM Triiodothyronine with media being replaced every 48 hours for up to 23 days.

The cells were subsequently washed in PBS and fixed using 4% (w/v) paraformaldehyde and stored at 4 degrees in PBS/50 units/ml penicillin/streptomycin prior to CARS analy-

sis. The cells were routinely screened for mycoplasma using the VenorGeM Mycoplasma Detection kit (Cambio, Cambridge, UK).

Spectral extrapolation for field retrieval algorithms

The fast Fourier transform (FFT) assumes a periodic data set, but the CARS intensity ratio spectra $\bar{I}_{\mathrm{C}}$ are not periodic. We create an input vector for FFT which suppresses the resulting artifacts by extrapolating the CARS intensity ratio to zero frequency with a constant equal to the measured $\bar{I}_{\mathrm{C}}$ at the lowest measured frequency. We use a frequency step given by the experimental spectral step and we interpolate, if needed, the measured $\bar{I}_{\mathrm{C}}$ to an even spacing of the frequency including zero. We then mirror the frequency range to negative frequencies, resulting in N_1 frequency points. To avoid wrap-around effects, we then extend the length of the vector to $N = 2^m$ elements symmetric around zero frequency, where m is chosen as the smallest integer so that $N > 2N_1$. This extension uses the constant value of the maximum measured frequency. The resulting periodic spectrum is continuous.

Details of the iterative Kramers-Kronig (IKK) method

The IKK method uses the self-consistency iteration

$$\bar{\tilde{\chi}}_{\mathrm{v}}^{\{i+1\}} = \alpha \mathcal{F}(\tilde{\theta}(t)\mathcal{F}^{-1}((\bar{I}_{\mathrm{C}} - |\bar{\tilde{\chi}}_{\mathrm{v}}^{\{i\}}|^2 - |\bar{\tilde{\chi}}_{\mathrm{e}}^{\{i\}}|^2)/|\bar{\tilde{\chi}}_{\mathrm{e}}^{\{i\}}|) + (1-\alpha)\bar{\tilde{\chi}}_{\mathrm{v}}^{\{i\}}, \tag{1}$$

with loop index $i = 0, 1, ..$ and damping factor α. During the iterations the RMS $\sigma^{\{i\}}$ of the residual $\bar{I}_{\mathrm{C}} - \left(|\bar{\tilde{\chi}}_{\mathrm{v}}^{\{i\}}|^2 + |\bar{\tilde{\chi}}_{\mathrm{e}}^{\{i\}}|^2 + 2\Re\left(\bar{\tilde{\chi}}_{\mathrm{v}}^{\{i\}}\bar{\tilde{\chi}}_{\mathrm{e}}^{\{i\}}\right)\right)$ over the measured spectral region is used to evaluate the convergence, which is estimated by the ratio $r = \sigma^{\{i+1\}}/\sigma^{\{i\}}$. We found that using $\alpha = 1$, i.e. without convergence control, the iteration can fail to converge for $|\bar{\tilde{\chi}}_{\mathrm{v}}/\bar{\tilde{\chi}}_{\mathrm{e}}| \leq 2$. We therefore use $\alpha<1$, and we initialize α with 0.1..0.8, higher for smaller resonant contributions. During iteration we control the convergence by adjusting α in the following way. If $r > 1$, α is changed according to $\alpha^{\{i+1\}} = (\alpha^{\{i\}})^{\beta_+}$, otherwise $\alpha^{\{i+1\}} =$

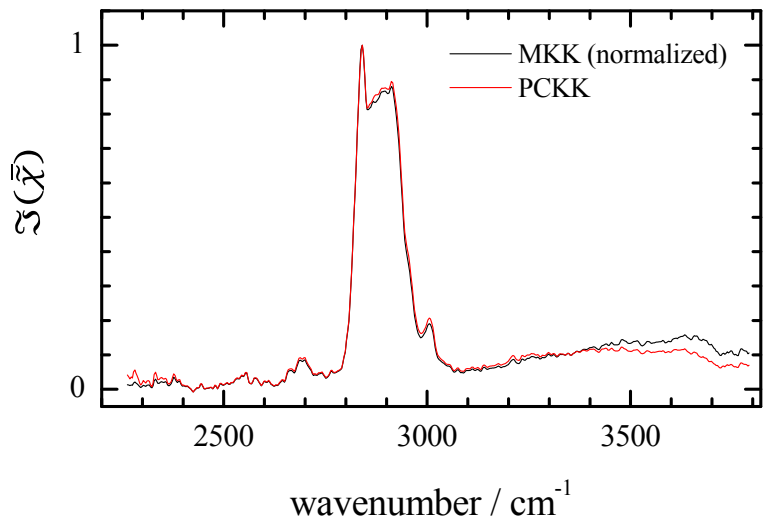

Figure S1: Retrieved imaginary part of the susceptibility in a lipid droplet using MKK (in arbitrary units, normalized, black line) and PCKK (red line).

$(\alpha^{\{i\}})^{\beta_-}$. The parameters β_+ and β_- control the speed of convergence control and were set to 1.2 and 0.98, respectively. The iteration of Eq.(5) proceeds sequentially through three phases, with the value of α reset to the initial value at the beginning of each phase. Each phase ends after n iterations without improvement of σ, where $n = 3$ was chosen. In phase one, we set $\bar{\tilde{\chi}}_{\rm v}^{\{0\}} = 0$, and $\bar{\tilde{\chi}}_{\rm e}^{\{0\}}$ is set constant, equal to the value of $\sqrt{\bar{I}_{\rm C}}$ at the lowest measured frequency. In phase two, $|\bar{\tilde{\chi}}_{\rm e}|^2$ is set in each iteration loop to the spectral average of $\bar{I}_{\rm C} - |\bar{\tilde{\chi}}_{\rm v}|^2$. In phase three, $\bar{I}_{\rm C}$ in the spectral region outside the measurement is set to the self-consistent spectrum $|\bar{\tilde{\chi}}_{\rm v}|^2 + |\bar{\tilde{\chi}}_{\rm e}|^2 + 2\Re(\bar{\tilde{\chi}}_{\rm v}\bar{\tilde{\chi}}_{\rm e}^*)$. The $\bar{\tilde{\chi}}_{\rm v}$ and $\bar{\tilde{\chi}}_{\rm e}$ returned by the algorithm are the ones with the lowest σ during iteration.

Use of CARS reference in the MKK method

In the MKK method,[4] the phase ϕ of the susceptibility is calculated by generating a temporal response using the inverse Fourier transform (IFT) of $\ln\left(\sqrt{I_{\rm C}}\right)$ for positive times and the IFT of $\ln\left(\sqrt{I_{\rm ref}}\right)$ for negative times. This is equal to using the IFT of $\ln\left(\sqrt{I_{\rm C}/I_{\rm ref}}\right)$ for positive times as in PCKK and thus provides a correction of ϕ for the effect of $I_{\rm ref}$, as we have analytically verified. However, in MKK a quantity proportional to the imaginary part of

the susceptibility is retrieved by multiplying $\sin(\phi)$ with $\sqrt{I_\mathrm{C}}$. This quantity is dependent on the instrument response $T(\omega)$. In PCKK instead, the retrieved susceptibility is normalized to the susceptibility of the reference medium, and is independent of $T(\omega)$. To illustrate the differences we show in Fig. S1 the comparison of the retrieved imaginary part of the susceptibility in a lipid droplet close to the CH_2 band using PCKK without phase correction (black line) and MKK (red line) normalized to the maximum of the PCKK result. The results deviate according to the specific $T(\omega)$ of our instrument.

Phase retrieval of simulated spectra

To verify the validity of the phase retrieval methods IKK and PCKK and compare their performance with the methods MKK and MEM reported in the literature, we first use simulated spectra exactly adhering to the assumptions of the methods. We use the susceptibility

$$\bar{\tilde{\chi}} = 1 + \sum_{j=1}^{5} \frac{2\alpha_j \sigma \omega_j}{\omega_j^2 - \omega^2 + 2i\sigma\omega}, \tag{2}$$

and as example choose a linewidth $\sigma/c = 10\,\mathrm{cm}^{-1}$, the resonance frequencies $\{\omega_j\}/(2\pi c) = \{1700, 1850, 2850, 2870, 3050\}\,\mathrm{cm}^{-1}$, and the amplitudes $\{\alpha_j\} = \{0.25, 0.5, 1, 1, 2\}$. The simulated ω range covers $-\omega_\mathrm{m}$ to ω_m with $\omega_\mathrm{m}/(2\pi c) = 4000\,\mathrm{cm}^{-1}$, and we use a step size of $0.2\,\mathrm{cm}^{-1}$ in the FFT.

The spectrum of the simulated $\bar{I}_\mathrm{C} = |\bar{\tilde{\chi}}|^2$, is shown in Fig. S2a, together with the imaginary parts $\Im(\bar{\tilde{\chi}})$ retrieved with MKK,[4] MEM,[5] IKK, and PCKK. The MEM retrieval was performed using the tool available.[6] For the MKK method, which uses $I_\mathrm{C} = \bar{I}_\mathrm{C} T |\tilde{\chi}_\mathrm{ref}|^2 |\bar{\tilde{\chi}}|$, we assume a frequency-independent T and $|\tilde{\chi}_\mathrm{ref}|$. The retrieval methods are applied to the extended spectrum as described in the supplement, except for MEM where we use a single-sided frequency range which resulted in a smaller error. The deviation Δ of the retrieved $\Im(\bar{\tilde{\chi}})$ from the exact $\Im(\bar{\tilde{\chi}})$ given by Eq.(2) is shown in Fig. S2c. Off resonance, a weakly frequency dependent Δ is found for all methods, which increases with wavenumber. The re-

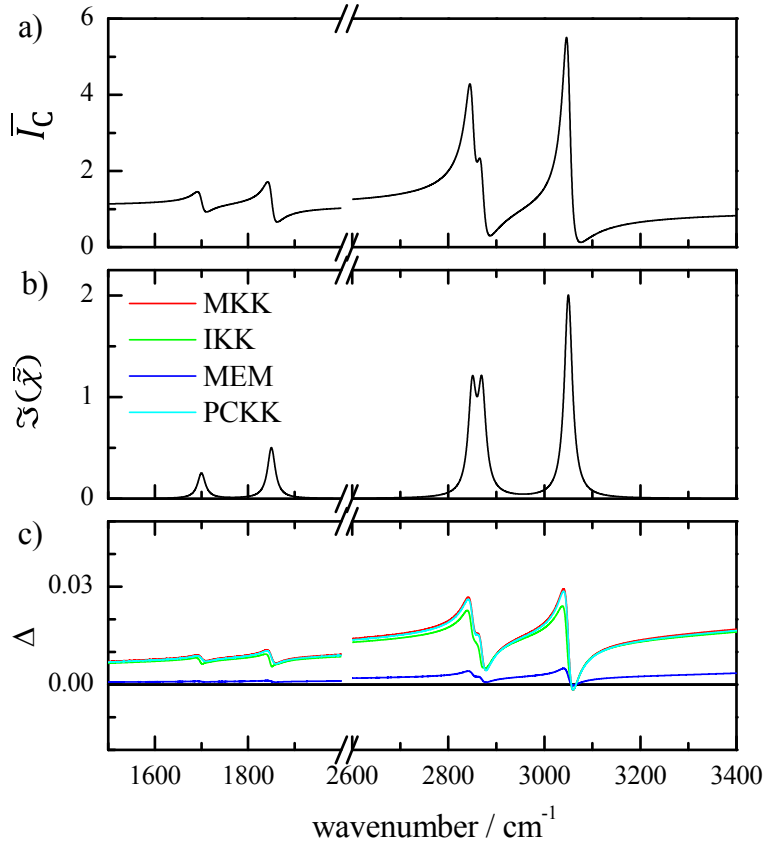

Figure S2: Phase retrieval of simulated CARS intensity data. a) $\bar{I}_{\mathrm{C}}$ according to Eq.(2). b) $\Im(\bar{\tilde{\chi}})$ according to Eq.(2). c) Deviation Δ of the retrieved $\Im(\bar{\tilde{\chi}})$ for the different methods as labeled.

trieval of the amplitude of the resonances become less accurate as the CARS ratio increases. The MKK and PCKK methods coincide since T is constant and the phase offset correction is zero due to the inclusion of zero frequency. We have also studied the dependence of the phase retrieval on the spectral range considered, as detailed in the SM Fig. S3 to Fig. S5. In general, a smaller spectral range introduces larger deviations. However, the errors are in the percent range which is typically below the noise in experimental spectra, and they are thus not a major limitation. In essence, all methods lead to an acceptable result for this simulation, with the MEM and PCKK showing the smallest errors. The fastest method is PCKK since it uses only a double Fourier transform operation.

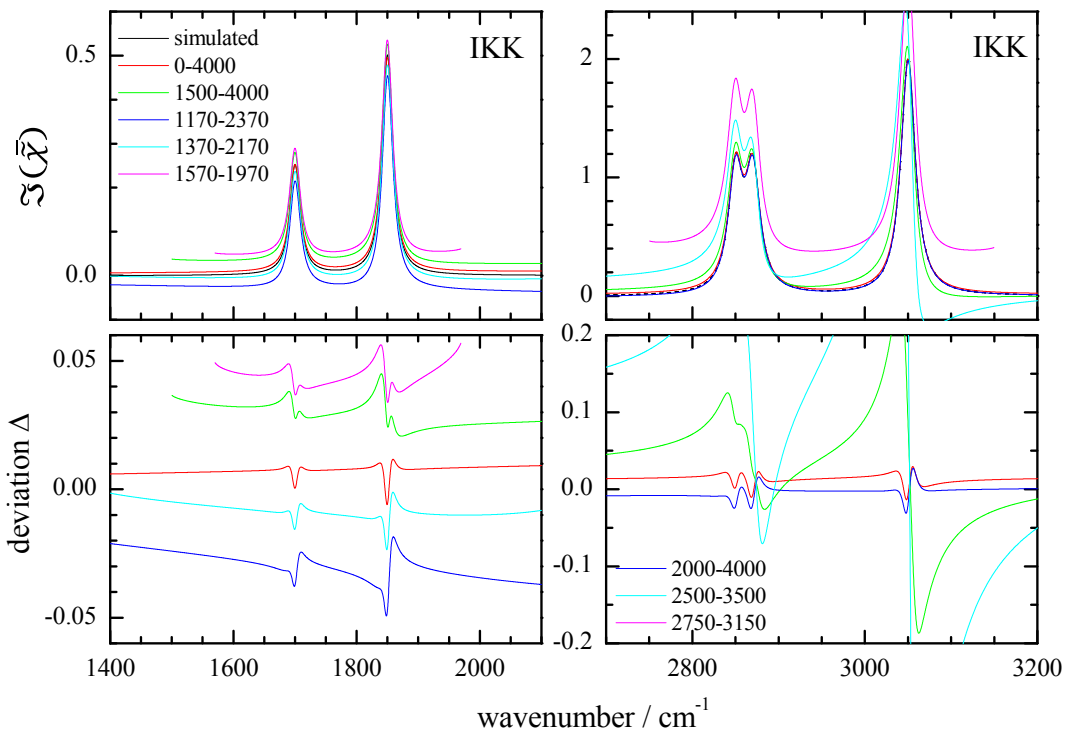

Figure S3: Top: Imaginary part of simulated susceptibility $\Im(\bar{\tilde{\chi}})$, and the corresponding IKK retrieved $\Im(\bar{\tilde{\chi}})$ using $\bar{I}_{\mathrm{C}}$ over restricted frequency ranges as indicated in cm^{-1}. Bottom: Deviation Δ between the retrieved and simulated $\Im(\bar{\tilde{\chi}})$.

Phase retrieval versus width of measured spectral range

Phase retrieval is a spectrally nonlocal operation and thus depends on the spectral range over which the CARS ratio $\bar{I}_{\mathrm{C}}$ is known. The different retrieval methods for the susceptibility for a simulated spectrum were compared in the main manuscript for a frequency range of 0-4000 cm^{-1}. In experiments, the measured frequency range is limited due to excitation and detection constraints, as well as measurement duration limitations. It is therefore relevant to discuss the influence of the measured frequency range on the retrieval fidelity for the different methods, which is shown in Figs. S3-S5, using the procedures discussed in the main manuscript. In general, all used retrieval methods produce an estimate of $\Im(\bar{\tilde{\chi}})$ with an error increasing with decreasing wavevector range, in particular for resonances with large $|\bar{\tilde{\chi}}_{\mathrm{v}}|/|\bar{\tilde{\chi}}_{\mathrm{e}}|$. Notably, IKK is most sensitive to the reduction in spectral range. PCKK and MEM show a similar error, with the peculiar property that the retrieval is best for a somewhat limited

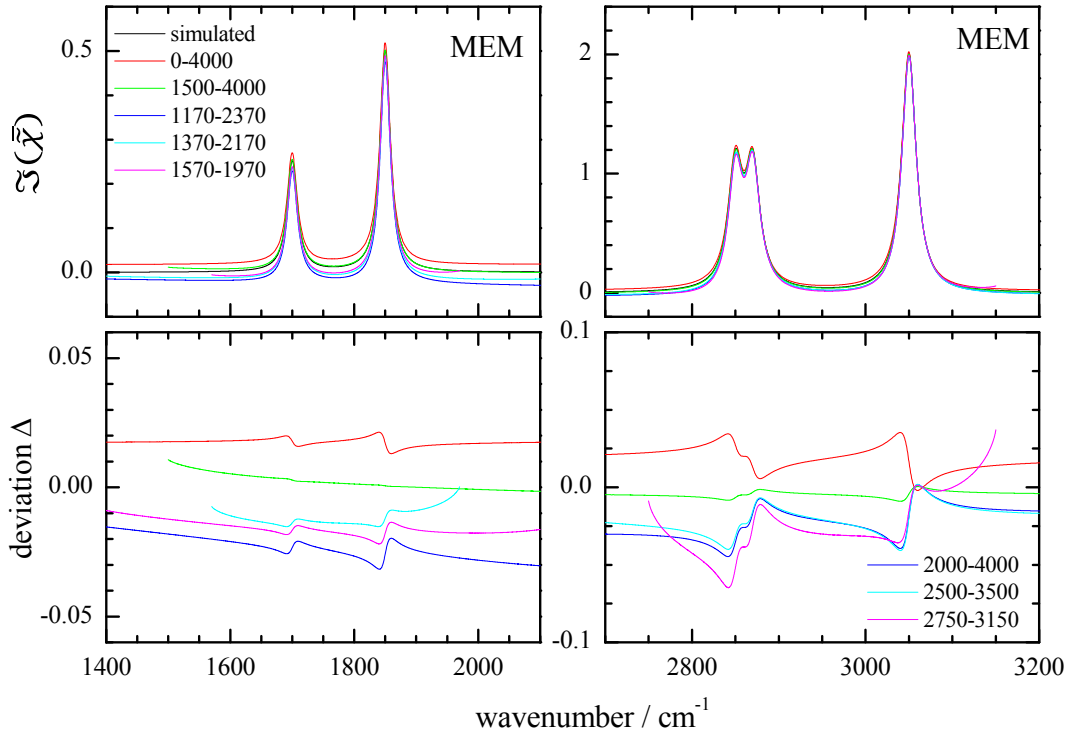

Figure S4: As Fig. S3 but retrieved by MEM.

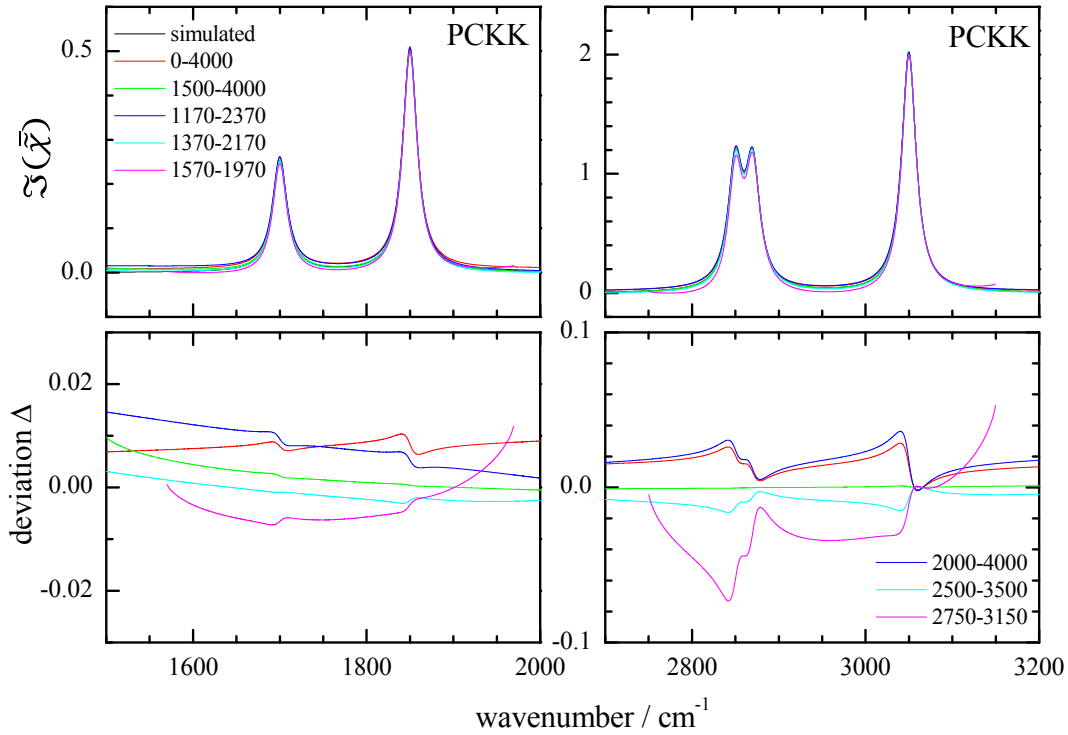

Figure S5: As Fig. S3 but retrieved by PCKK.

frequency range.

Unbiased noise reduction using SVD

The filtering of noise using SVD is based on the determination of the number of singular vectors which contain significant information. Different protocols have been discussed in literature,[7] for example based on the observation of a significant change in the slope of the diagonal elements of $\mathbf{\Sigma}$, or considering a manual threshold in the first-order autocorrelation function for the columns of $\mathbf{U}$ and $\mathbf{V}$, or by determining the components which reconstruct a matrix $\mathbf{D}_{\mathrm{nf}}$ with random residuals of the difference $\mathbf{D}-\mathbf{D}_{\mathrm{nf}}$. We propose here an unbiased method to determine the maximum number $i_{\max}$ of singular values with significant information. To motivate the approach, we consider SVD of a $S \times P$ matrix of random numbers with a Gaussian distribution with zero mean and unity standard deviation. Fig. S6a shows the resulting singular values for different P and $S = 500$. The dependence on the index i is approximately linear. We fit the singular values $\mathbf{\Sigma}_{i,i}$ with a linear function $A - iB$. The slope B and the relative error of the fit $\varepsilon = (\mathbf{\Sigma}_{1,1} - A - B)/\mathbf{\Sigma}_{1,1}$ is given in Fig. S6b as function of the P and S. We find that $\varepsilon \sim 0.2(S/P)^{3/4}$ and $B \sim 1.8/\sqrt{S}$. The linear fit is suited for $P \gg S$, which is satisfied by typical experimental conditions of $S < 1000$ and $P \sim 20000$, resulting in an error $\varepsilon < 5\%$. We can use this finding on data which have a whitened noise contribution which is therefore described by this simulation. Assuming that at least half of the singular values are dominated by noise, we can estimate the noise contribution to all singular values by a linear fit to the singular values with $i > S/2$ which are noise dominated. Singular values which contain a signal contribution larger than the noise then have a value larger than $\sqrt{2}$ times the noise value estimated by this fit. We therefore define $i_{\max}$ as the largest number for which the singular values up to $i_{\max}$ are larger than $\sqrt{2}$ times the fit, *i.e.* they contain a signal contribution larger than the estimated noise.

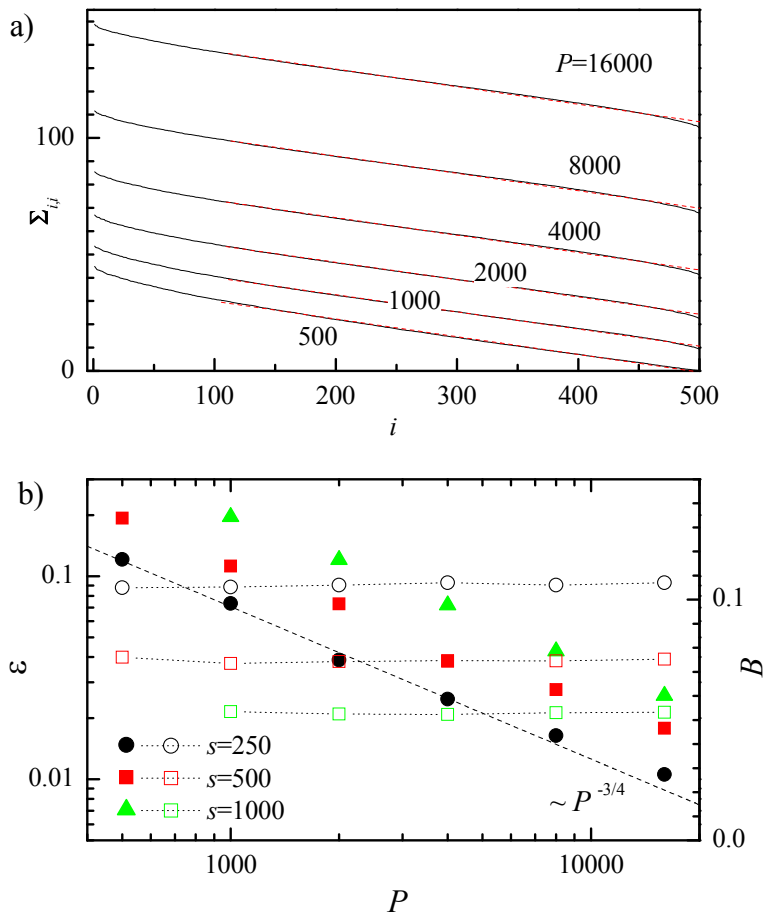

Figure S6: a) Singular values of a $500 \times P$ matrix of random numbers with a Gaussian distribution of zero mean and unity standard deviation. b) relative error ε (full symbols) and slope B (empty symbols) as function of P for different values of S as given. The dashed line shows a $0.2 \times (250/P)^{3/4}$ dependence.

Phase retrieval of a measured lipid droplet spectrum

Fig. S7 shows the $\bar{I}_{\mathrm{C}}$ and retrieved $\Im(\bar{\tilde{\chi}})$ spectra of a large lipid droplet measured in a 3T3L1-derived adiptocyte. The corresponding area is indicated by the red circle in Fig. S9. Similarly to the case of PS and GTO, the IKK, MKK and MEM methods retrieve a $\Im(\bar{\tilde{\chi}})$ with a negative offset, which is corrected in the PCKK method. The different methods are able to retrieve all the resonances visible in the Raman spectrum, and also the amplitude ratios between the resonances are approximately reproduced. The stronger water resonance around $3300\,\mathrm{cm}^{-1}$ from the surrounding medium visible in the Raman spectrum is attributed to the weaker optical sectioning in the confocal Raman data.

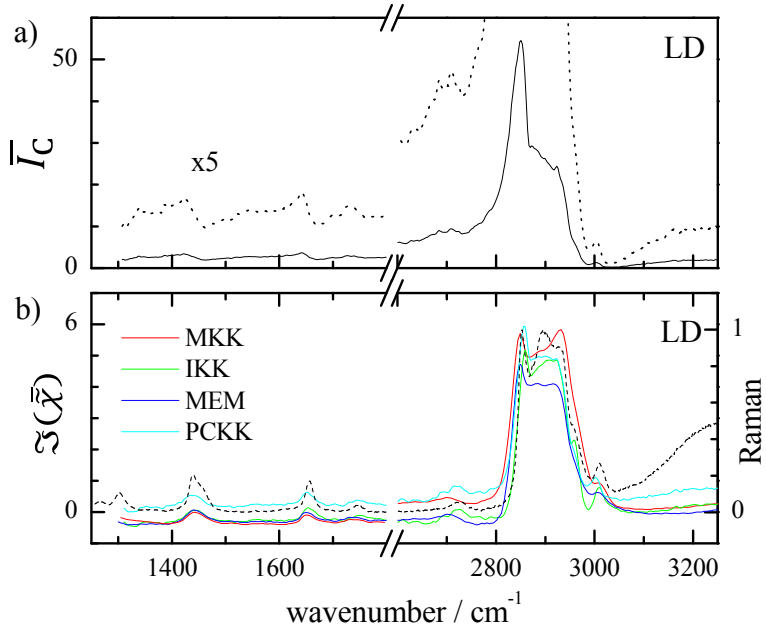

Figure S7: a): CARS intensity ratio measured in the lipid droplet and retrieved $\Im(\tilde{\chi})$ (b) with the Raman spectrum (dashed).

Determination of the absolute concentration of chemical components using MCR

The MCR analysis used in Ref. 8 is an existing alternative to FSC[3] to factorize hyperspectral data in order to obtain quantitative information on the chemical composition of the investigated sample. Fig. S8a shows the results of the MCR method on the hyperspectral $\Im(\tilde{\chi})$ images measured in the octanoic and α-linolenic acid mixture series of Fig. 2. In the analysis we used the MCR-ALS Matlab toolbox [9] as in Ref. 8, where two components were considered, constraints were set for non-negative spectrum and concentration values and for sum of the concentrations to be equal to 1, and convergence to 0.01% was requested. The dashed lines represent the spectra of the pure lipids, while the solid lines are the spectra obtained by MCR using random spectra and concentrations given by a uniform distribution between zero and one as initial guess. We found that the MCR results are dependent on the initial spectra, and we therefore represent the spectra as averages with error bars given by plus and minus their standard deviation over random initial spectra and concentrations.

The error is specifically evident in the α-linolenic acid spectrum, corresponding to the second MCR component, around the peak at $3020\,\mathrm{cm}^{-1}$. The resulting concentrations of the components are shown in the inset versus the nominal concentration, again with the error bars representing plus and minus their standard deviation over random initial spectra and concentrations. The MCR concentrations deviate significantly from the nominal ones, with errors in the 20% range. This is about an order of magnitude larger than for FSC^3 (see Fig. 2), and the FSC^3 method also does not show a significant dependence on the initial spectra and concentrations, with a standard deviation of about 10^{-4} in the concentration over random initial spectra and concentrations. Similar results are obtained using MCR on Raman data as shown in Fig. S8b. In terms of computational effort MCR is about two orders of magnitude slower than FSC^3. A possible reason for the stronger fluctuations of the MCR results is that it uses the concentration constrain explicitly in the minimization algorithm. Any spatially dependent variation in the signal created for example by the refractive index structure of the signal is disturbing the retrieved spectra. In the FSC^3 method we only rescale the concentrations and spectra globally to minimize the variation of the sum of concentrations from 1 over the whole image, which is not having an explicit influence on the retrieval of the spectra. We can therefore conclude that in typical experimental datasets the spatial intensity variations are too strong to use the concentration constrain explicitly for the spectra retrieval.

Instead of using random initial spectra, they can be obtained by using the evolving factor analysis (EFA) algorithm available within the MCR toolbox. EFA provides estimates for the concentration matrix which can be used to initialize the MCR analysis. However the EFA algorithm is computationally even slower than MCR so that only a sub-ensemble of the data can be analyzed within a reasonable time. The obtained estimation of the sub-ensemble concentration matrix can be used to run the MCR analysis to find a set of spectra which can be used than as initial guess for the MCR on the full dataset. The choice of the sub-ensemble is important, as it has to be statistical relevant and unsupervised. We used 10%

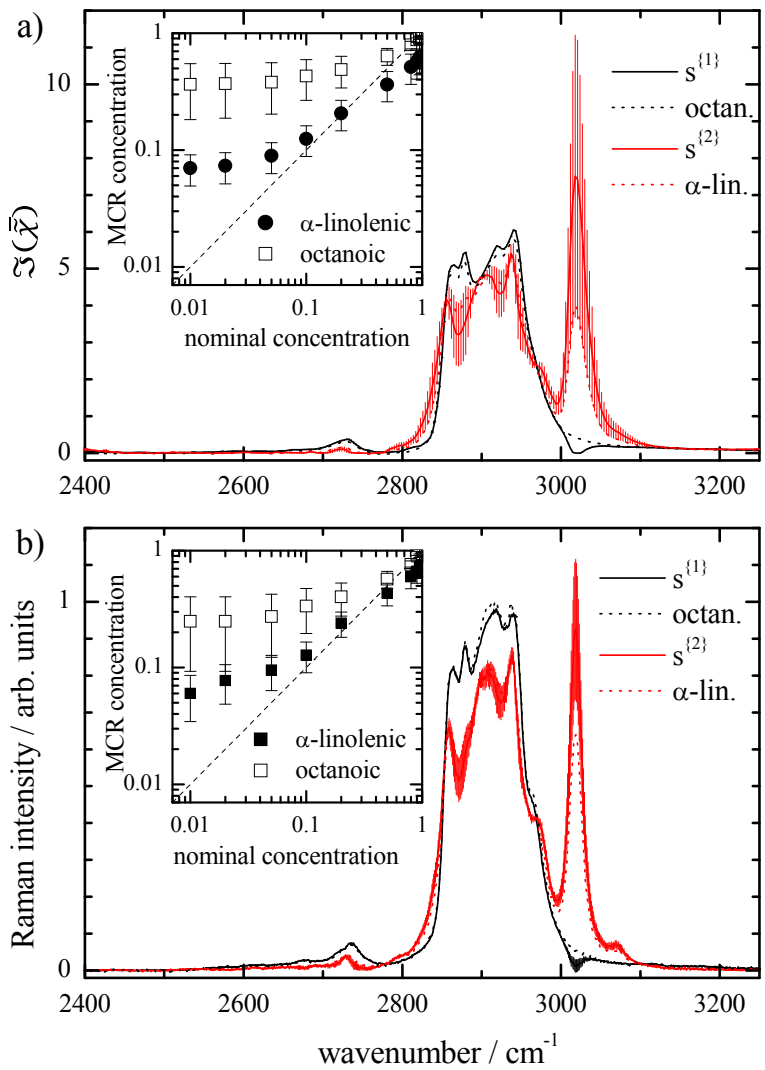

Figure S8: a) MCR $\Im(\bar{\tilde{\chi}})$ spectra $s^{\{k\}}$ (solid lines) of mixtures of octanoic and α-linolenic acid, compared with the spectra of the pure compounds (dashed lines). Inset: FSC^3 concentrations $c^{\{k\}}$ versus nominal concentration (v/v). The error bars are given by the standard deviation over random initial spectra. b) as a) for Raman spectra.

of the original data at randomly selected spatial points. The combined EFA-MCR method is $\sim$ 200 times slower than the FSC^3 method, and gives results similar to FSC^3. Other initialization methods such as non-negative SVD, selecting the most dissimilar spectra, etc., are described in literature, but require more computational effort. In Ref. 8 MCR was used with the measured spectra of the known pure substances as initial estimate.

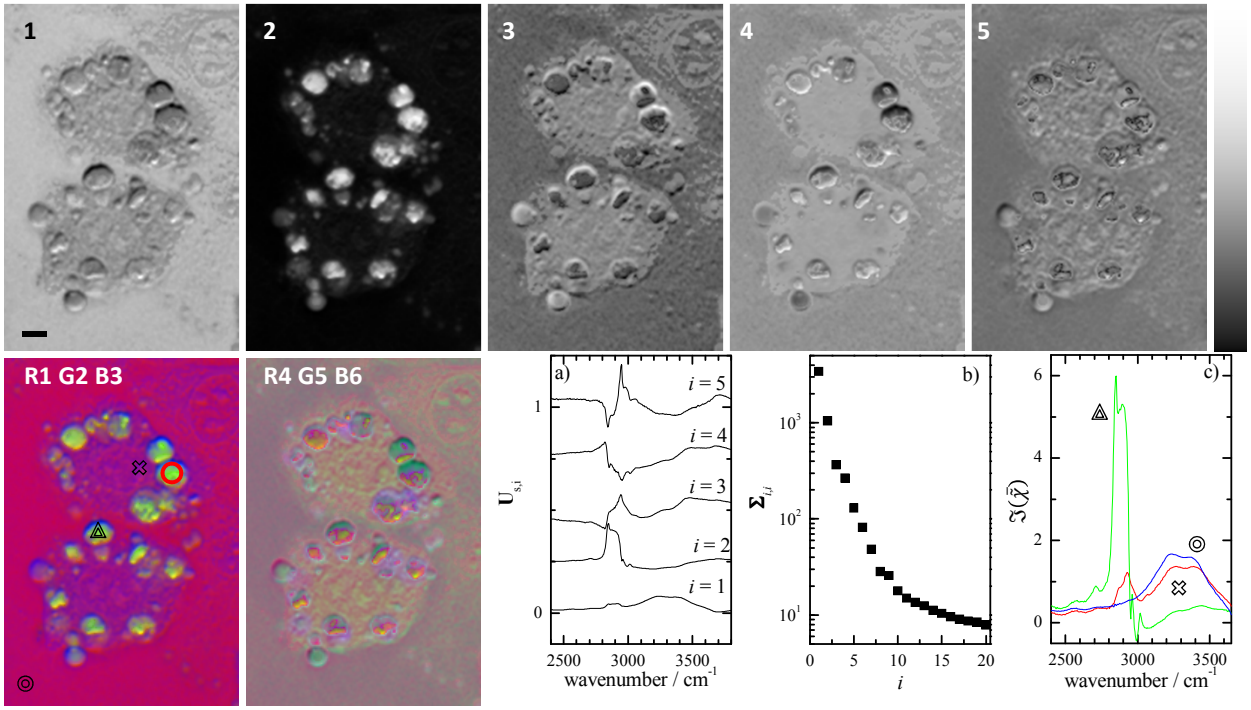

Figure S9: As Fig. 4 but for $\Im(\bar{\tilde{\chi}})$ retrieved by IKK. The scale bar indicates 5 μm.

SVD analysis on hyperspectral $\sqrt{I_{\mathrm{C}}}$ and IKK-retrieved $\Im(\bar{\tilde{\chi}})$ images

Images of the first five singular values of the SVD of $\Im(\bar{\tilde{\chi}})$, retrieved using the IKK method, are shown in Fig. S9. The first three components are similar to the ones for PCKK (see Fig. 4). The fourth component shows an inverted contrast compared to PCKK results, while the fifth component is different, showing spatially localized maxima and minima. Analysis of this behaviour showed that the iterative nature of the IKK can produce spurious parts due to limited convergence, which can be above the noise of the data and thus visible in the higher SVD components. This is specifically relevant at sharp spatial structures where spectral artifacts can appear due to the sequential acquisition of the spectra.

In the SVD images of $\sqrt{I_{\mathrm{C}}}$ shown in Fig. S10, the lipid droplets are surrounded by thin layer of a different singular component. This is an result of the interference between χ_{e} and χ_{v} in $\sqrt{I_{\mathrm{C}}}$. In the corresponding images of $\Im(\bar{\tilde{\chi}})$ (see Fig. S9 for IKK and Fig. 4 for PCKK

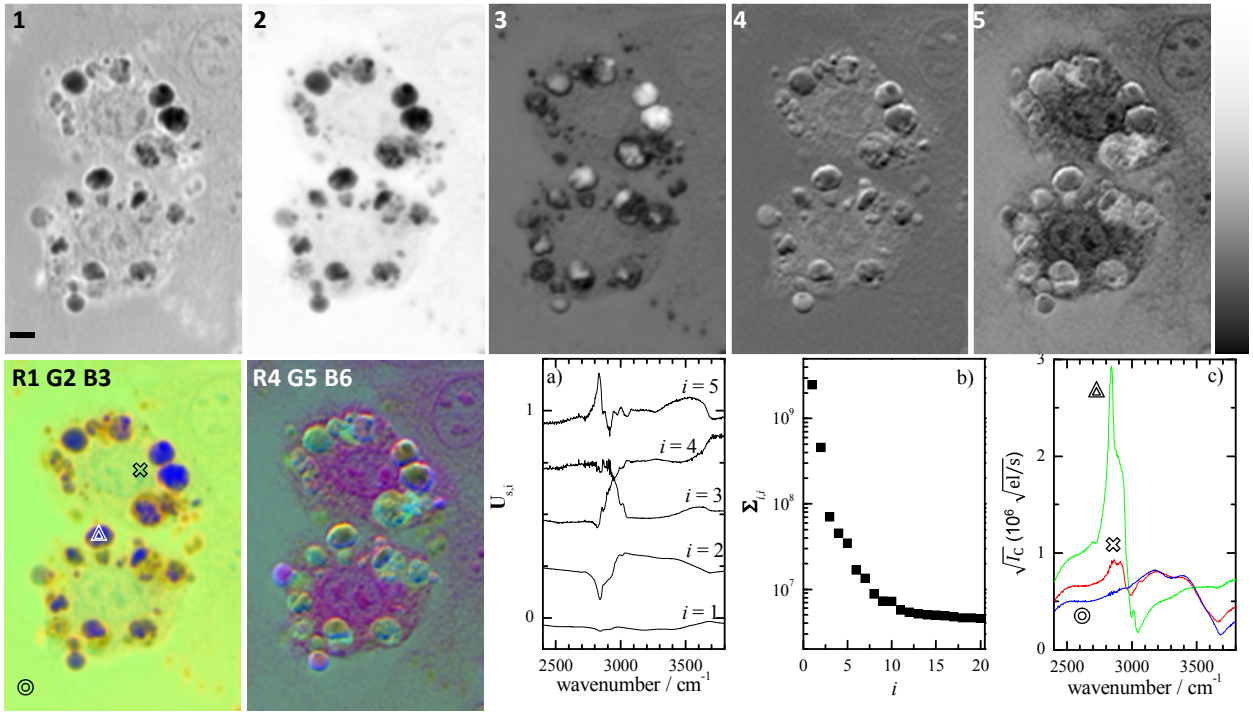

Figure S10: As Fig. 4 but for $\sqrt{I_C}$. The scale bar indicates 5 μm.

retrieval), this artifact is removed and the lipid droplets are homogeneous in color indicating a homogeneity in the chemical composition.

SVD basis rotation

The SVD spectra of $\Im(\tilde{\chi})$ do not correspond to individual chemical components, but rather to differences between chemical components fluctuating independently. The SVD analysis and subsequent visualization helps to determine regions of the samples which present the same color and that can be identified as a single substance. Once a substance is identified one can project the first vector of the matrix $\mathbf{U}$ onto the defined spectrum and generate a new set of vectors as new basis for the spectra. To do that we calculate an average spectrum in a manually defined spatial region representing one substance. We rotate $\mathbf{U}$ to $\mathbf{U}' = \mathbf{UR}$ with the rotation matrix $\mathbf{R}$ such that the rotated basis $\mathbf{U}'$ has a first vector given by this spectrum. The spatial distribution of the new basis vectors is then given by $\mathbf{D}' = (\mathbf{U}')^{-1}\mathbf{D}$.

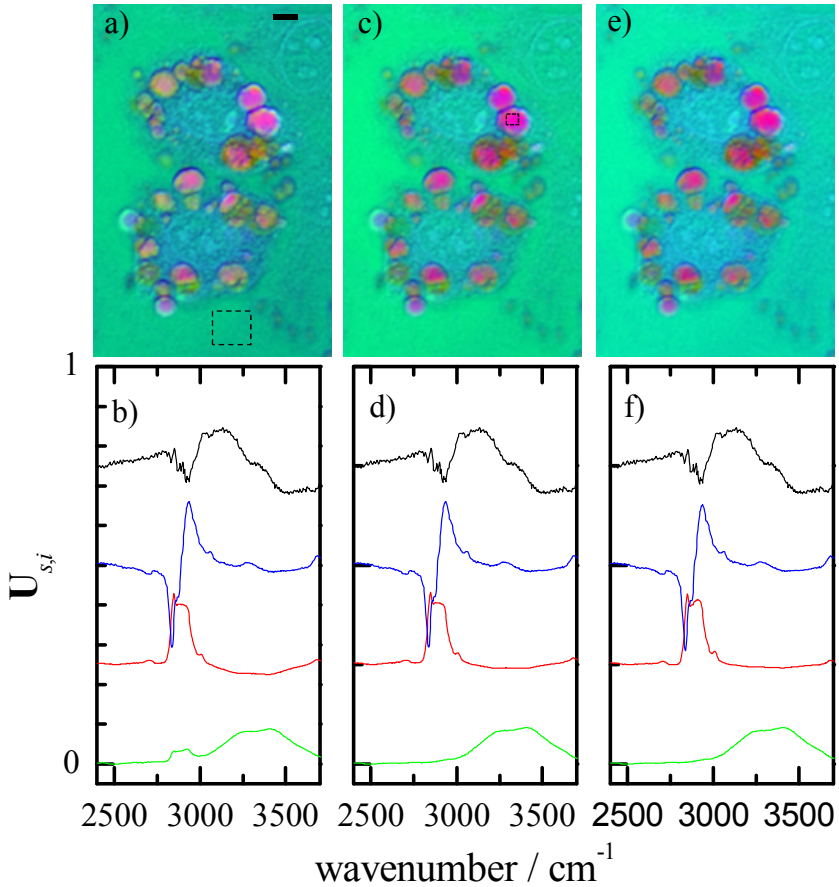

Figure S11: a),b) Reconstructed color images of $\mathbf{\Sigma V}^{\mathrm{T}}$ and left spectra of $\mathbf{U}$ after SVD on $\Im(\bar{\tilde{\chi}})$ retrieved as in Fig. 4. c),d) after rotating to $\mathbf{U}$' align the first left vector with the average spectrum in the rectangular region indicated in a). e),f) after rotating $\mathbf{U}$' to additionally project the second left vector onto the lipid spectrum calculated as average spectrum in the rectangular region shown in in c).

This rotation process of $\mathbf{U}$' can be repeated in the remaining subspace i.e. excluding the already projected dimensions, until all left vectors of $\mathbf{U}'$ are determined. We limit this operation to the first $i_{\max}$ components of $\mathbf{U}$, i.e. the ones containing signal above noise. We show an example in Fig. S11, where panel a) gives the color reconstructed $\mathbf{\Sigma V}^{\mathrm{T}}$ image after SVD analysis of $\Im(\bar{\tilde{\chi}})$ with the corresponding singular spectra in b). Since the region outside the cells is dominated by water, we project the first vector of $\mathbf{U}$ onto this spatial region (indicated with solid lines in Fig. S11a), resulting in the $\mathbf{D}'$ displayed in Fig. S11b. In the resulting first vector of $\mathbf{U}'$ (see Fig. S11d) the lipid band at $2850\,\mathrm{cm}^{-1}$ is suppressed. We then project the second vector of $\mathbf{U}$' onto the spectrum measured on a lipid droplet (see

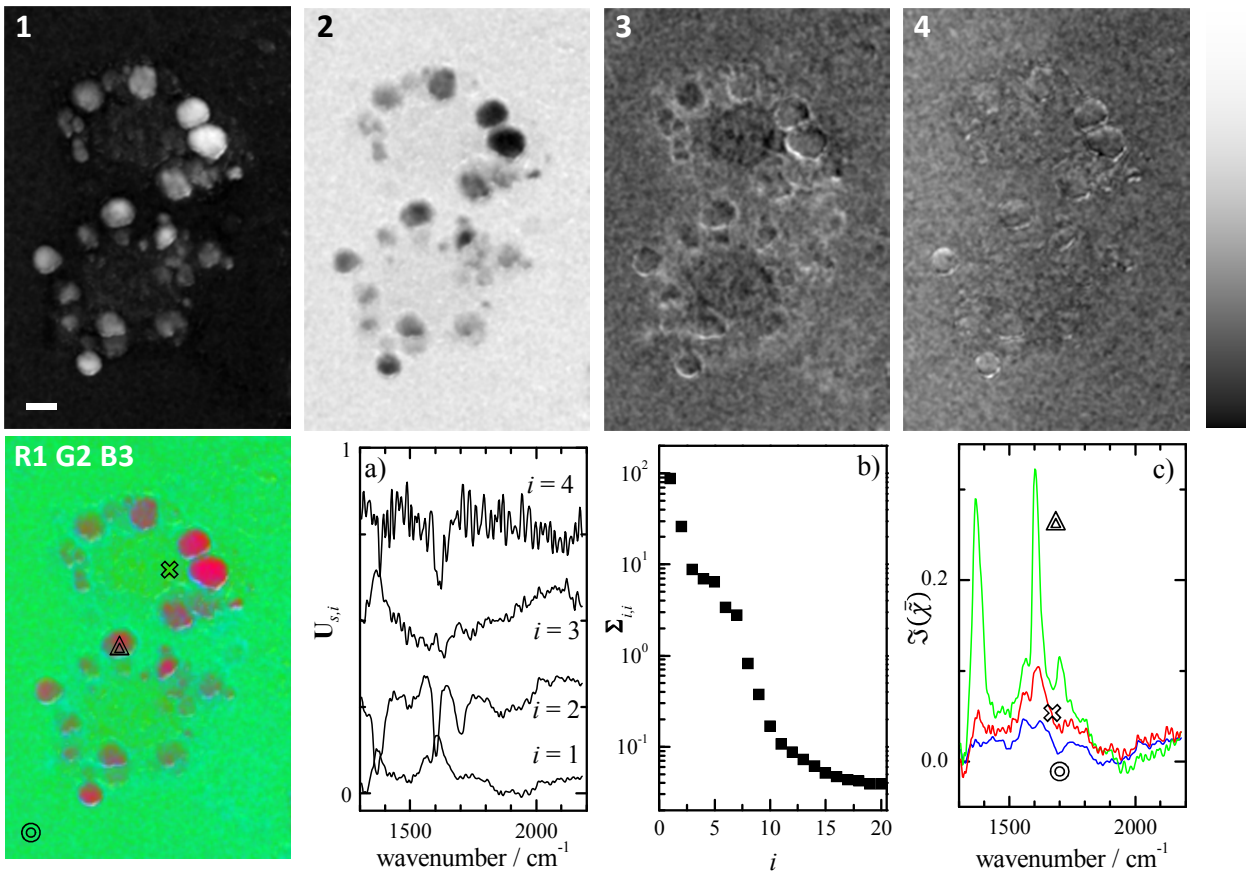

Figure S12: Same as Fig. S10 for $\Im(\bar{\tilde{\chi}})$ hyperspectral images of 3t3l1-derived adipocytes in the 1300-2200 cm^{-1} range retrieved using PCKK. The scale bar indicates 5 μm.

solid line in c), reducing the inverse water band in the second vector of **U**'. The associated color image of **D**' (see Fig. S11e) shows an improved contrast between the substances (water, lipid, and cytosol).

FSC^3 analysis in the characteristic region

FSC^3 analysis has been performed on hyperspectral images of adipocytes taken in the characteristic region (1300-2200 cm^{-1}). Fig. S12 shows the reconstructed images after SVD on $\Im(\bar{\tilde{\chi}})$ retrieved by PCKK. The first component shows a distribution peaked at the lipid droplets, while the water surrounding the cells appears bright in the second component. The third component shows an inverted cell nucleous. The fourth component appears evenly dis-

tributed in the sample and can be considered as noise. The associated SVD spectra, namely the columns of $\mathbf{U}$, and the diagonal elements of $\mathbf{\Sigma}$ are displayed in panel a) and b), are consistent with the assignment by morphology. The SVD spectra of the first component shows the typical peaks associated with triglycerids. The second SVD spectrum shows dips in correspondence of the lipid resonances. The third spectrum shows a peak at $1370\,\mathrm{cm}^{-1}$. Fig. S13 shows the results of the FSC^3 analysis in the $1300 - 2200\,\mathrm{cm}^{-1}$ region into four chemical components. The first and the third components have opposite contrast and can be associated to water and lipid, respectively, with a volume fraction of 59% and 8%. The second component shows a double peak around $1600\,\mathrm{cm}^{-1}$ and has a volume fraction of 30% with a high concentration at the nucleoli and nucleus membrane. The fourth component accounts for the remaining volume fraction of 3% and shows an imaginary part dominated by spectral noise and shows the highest concentrations at the edge of the lipid droplets. It is attributed to motion and/or light propagation artifacts.

Similarly to what was observed in the high frequency region, the maximum error of the total concentration $\mathbf{E}_\mathrm{C}$ of about ± 0.2 is localized at the lipid droplet edges and in the largest lipid droplets. This is consistent with its origin being the optical aberration introduced by the variation of refractive index between the droplets and the cellular matrix, reducing the signal intensity and thus artificially increasing the concentration in the analysis. It is important to note that in this spectral region the component of highest average concentration, water, does not have any vibrational resonance, and can only bee seen due to the inclusion of $\hat{\chi}_{\mathrm{e}p}$ in the analysis. Indeed, using the NMF on $\Im(\bar{\tilde{\chi}})$ alone returns a large concentration error $\mathbf{E}_\mathrm{C}$ ranging from -0.4 to 2.1, and a lacking contrast of the nucleoli.

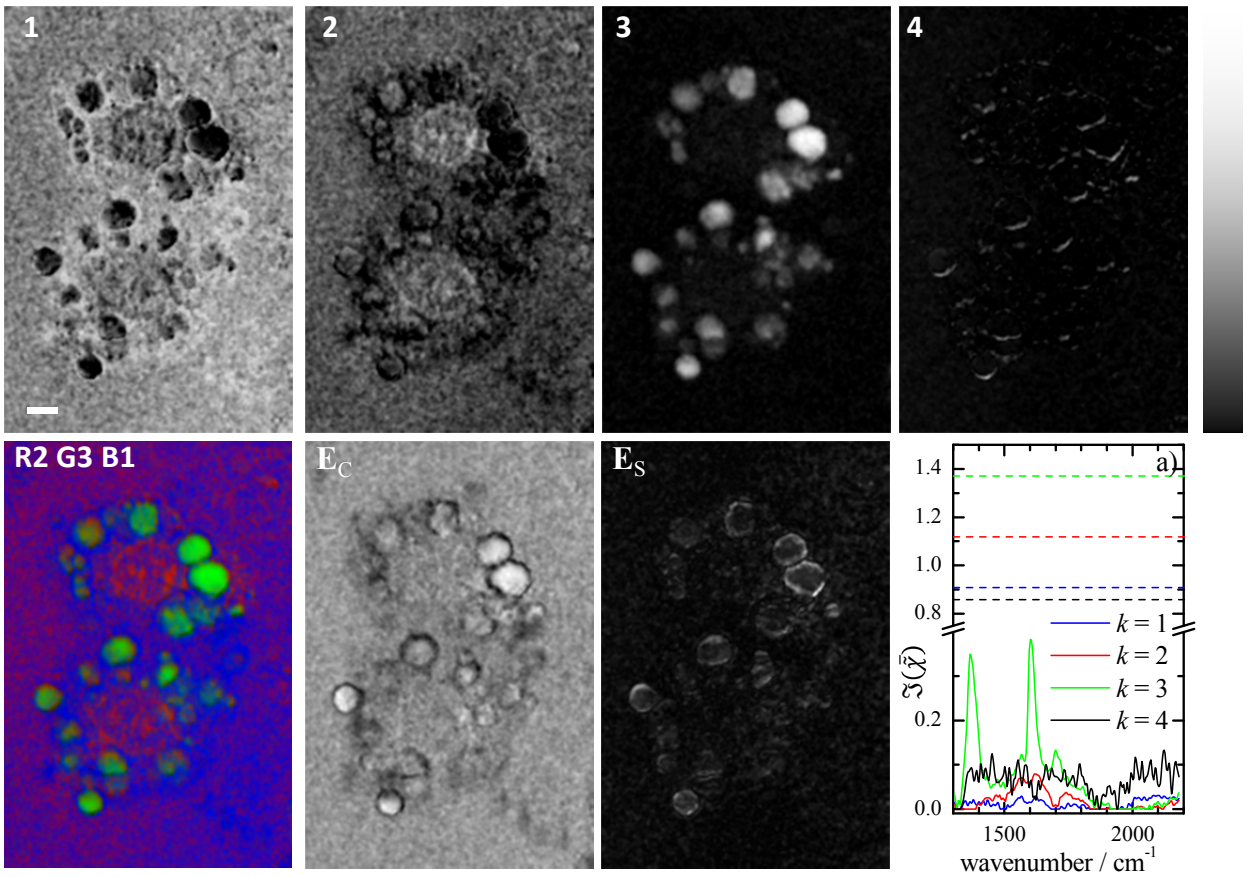

Figure S13: Results of the FSC^3 with $K = 4$ on $\Im(\bar{\tilde{\chi}})$ of adipocytes as Fig. 5, but using the 1300-2200 cm^{-1} range. Top: Spatial distribution of the concentration $\mathbf{C}$. The grayscale ranges from 0 to 1.14. The corresponding component spectra $\Im(\bar{\tilde{\chi}}^{\{k\}})$ are displayed in a) together with the spectrally averaged $\Re(\bar{\tilde{\chi}}^{\{k\}})$ (dashed lines). Bottom: reconstructed color images overlaying the $\mathbf{C}$ images using the third component as red, the first as green and the fourth as blue. The images of the three channels have been independently normalized to their maxima. $\mathbf{E}_C$ indicates the concentration sum matrix, with grayscale ranging from -0.2 to 0.16. The spectral error $\mathbf{E}_S$ spatial distribution is also shown with a grayscale ranging from 0.04 to 0.95. The scale bare indicates 5 μm.

SVD analysis of $\Im(\bar{\tilde{\chi}})$ of differentiated mouse embryonic stem cells

We show in Fig. S14 the SVD analysis of $\Im(\bar{\tilde{\chi}})$ from mouse embryonic stem cells which were exposed to the differentiation protocol but not exhibiting the morphology of mature adipocytes, for comparison with the FSC^3 results shown in Fig. S15. The reconstructed $\mathbf{\Sigma V}^{\mathrm{T}}$ images show clear differences in the spatial distribution of the SVD spectra $\mathbf{U}_{s,i}$. For

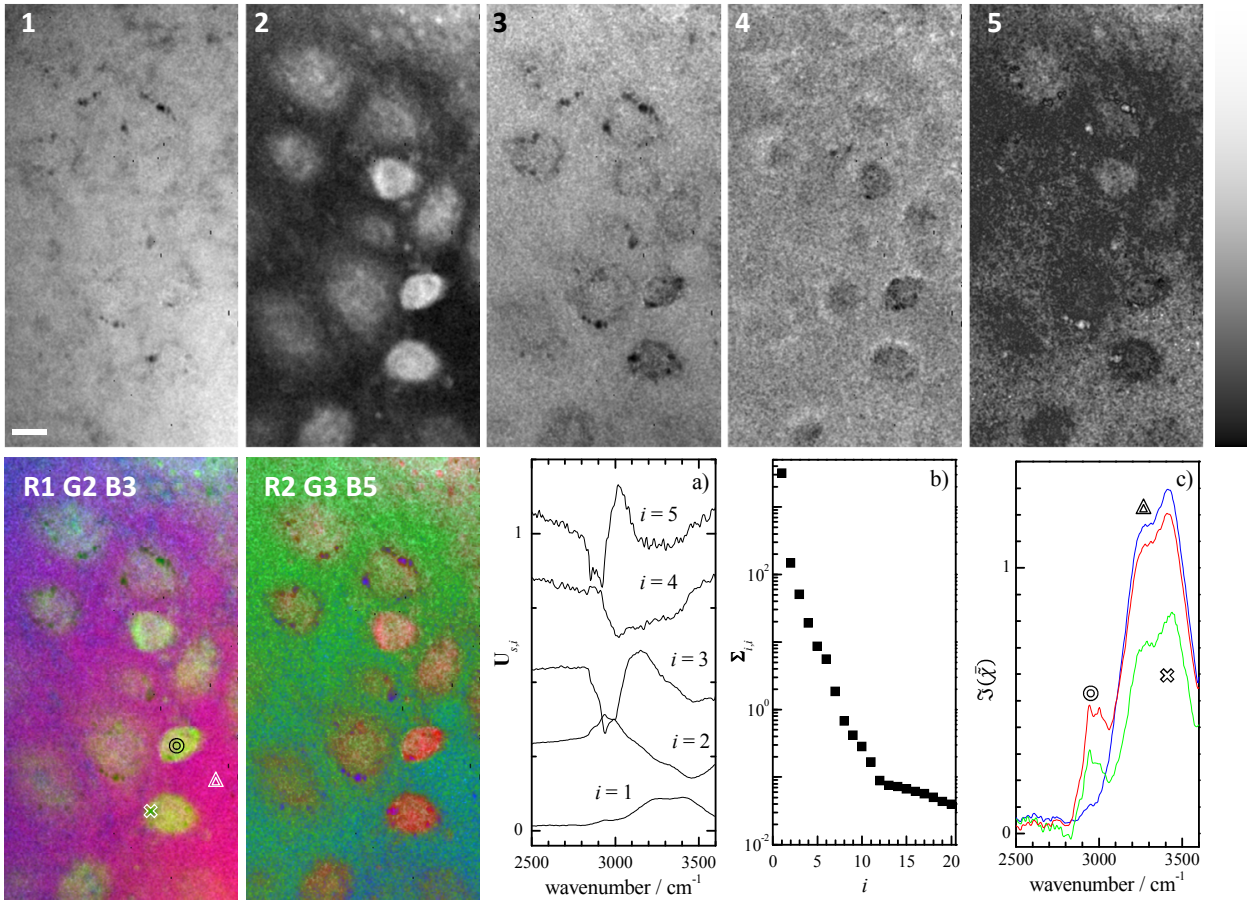

Figure S14: Same as Fig. S10 for $\Im(\tilde{\chi})$ hyperspectral images of a group of differentiated mES cells measured in the 2400-3600 cm^{-1}region. The scale bar indicates 10 μm.

example, the first singular value shows a distribution which is homogenous in the image, and can be associated to water background. The second component, instead, is localized in in the cell cytosol. The third and fourth component are maxima in the water and minima at the cells, while the fifth shows a strong intensity at the small droplets structures. Encoding the $\mathbf{\Sigma V}^{\mathrm{T}}_{i,p}$ with different colors help in the visualization of the contrast between water, droplets and cell cytosol. Similarly to what found for adipocytes, we are able to observe internal structure of the cytosol in spite of the smaller signal to noise ratio of the measured CARS intensity.

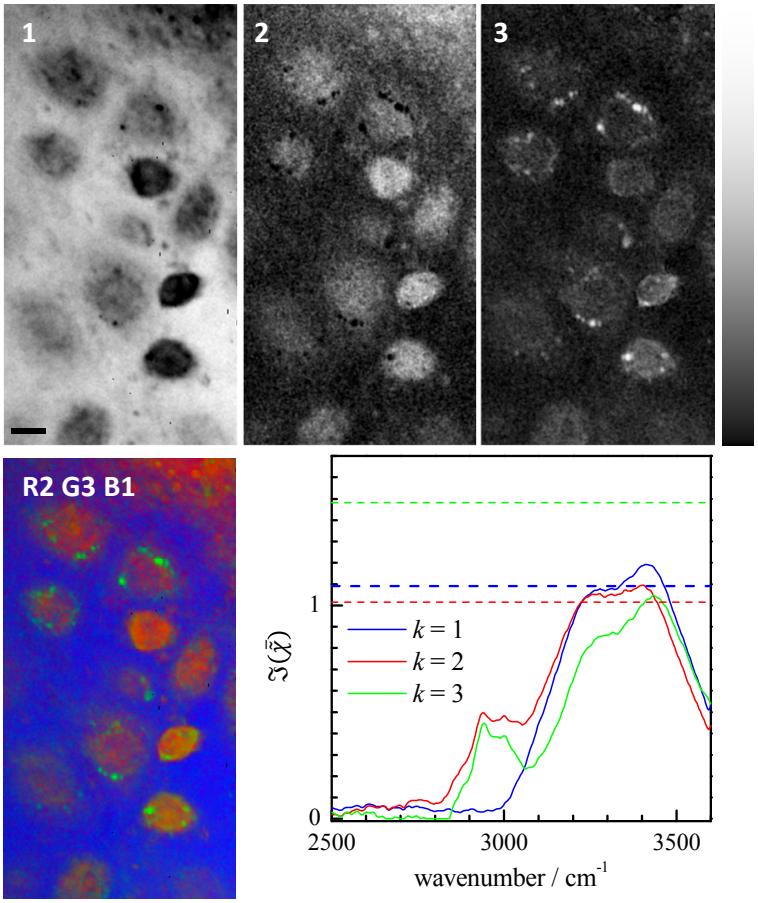

Figure S15: Results of FSC^3 on $\Im(\bar{\tilde{\chi}})$ retrieved by PCKK for a group of differentiated mES cells. The grayscale for the concentration images ranges from 0 to 1. The scale bar indicates 10 μm.

FSC^3 on differentiated mouse embryonic stem cells

The phase retrieval and FSC^3 analysis is also suited for samples with a weak resonant susceptibility, such as the cells of Fig. S15. The result of FSC^3 with $K = 3$ is given in Fig. S15. The identified components are separated into bulk water mostly outside the cells (1), a cytosolic component (2), and a third component similar to 2 but with a slightly different peak shape of both protein/nucleic acid and water resonances, and a significantly stronger non-resonant susceptibility. This component is spatially localized into micrometric structures/droplets. To interpret these results further other complementary biochemical techniques could be used.

Table of relevant symbols used

Symbol	Definition
$\tilde{\chi}$	CARS susceptibility in frequency domain
I_{C}	CARS intensity
$\mathcal{R}$	Instrument response
T	Transduction coefficient
$\mathcal{R}_{\mathrm{s}}$	Spectral broadening instrument response
$\tilde{\chi}_{\mathrm{e}}$	Non-resonant electronic contribution of the susceptibility in frequency domain
$\tilde{\chi}_{\mathrm{v}}$	Resonant vibrational contribution of the susceptibility in frequency domain
$\tilde{\chi}_{\mathrm{ref}}$	CARS susceptibility of a non-resonant medium in frequency domain
I_{ref}	CARS intensity of a non-resonant medium
$\bar{I}_{\mathrm{C}}$	CARS ratio, i.e. CARS intensity normalized to a non-resonant medium
$\bar{\chi}$	CARS susceptibility in time domain normalized to a non-resonant medium
$\bar{\tilde{\chi}}$	CARS susceptibility in frequency domain normalized to a non-resonant medium
$\bar{\tilde{\chi}}_{\mathrm{e}}$	Non-resonant electronic contribution of the normalized susceptibility
$\bar{\tilde{\chi}}_{\mathrm{v}}$	Resonant vibrational contribution of the normalized susceptibility

References

(1) McCreery, R. L. In *Handbook of Vibrational Spectroscopy*; Chalmers, J. M., Griffiths, P. R., Eds.; John Wiley & Sons Ltd, Chichester, 2002.

(2) Bierbaum, P.; Maclean-Hunter, S.; Ehlert, F.; Moroy, T.; Müller, R. *Cell Growth Diff* **1994**, *5*, 37–46.

(3) Dani, C.; Smith, A.; Dessolin, S.; Leroy, P.; Staccini, L.; Villageois, P.; Darimont, C.; Ailhaud, G. *J Cell Sci* **1997**, *110*, 1279–1285.

(4) Liu, Y.; Lee, Y. J.; Cicerone, M. T. *Opt. Lett.* **2009**, *34*, 1363.

(5) Vartiainen, E. M.; Rinia, H. A.; Müller, M.; Bonn, M. *Opt. Express* **2006**, *14*, 3622–3630.

(6) A tool for MEM calculations is available at *http://memcars.amolf.nl/*.

(7) Lee, Y. J.; Moon, D.; Migler, K. B.; Cicerone, M. T. *Anal. Chem.* **2011**, *83*, 2733–2739.

(8) Zhang, D.; Wang, P.; Slipchenko, M. N.; Ben-Amotz, D.; Weiner, A. M.; Cheng, J.-X. *Anal. Chem.* **2013**, *85*, 98–106.

(9) Jaumot, J.; Gargallo, R.; de Juan, A.; Tauler, R. *Chemom. Intell. Lab. Syst.* **2005**, *76*, 101 – 110.